Journal of Zhejiang University-SCIENCE A in press
www.jzus.zju.edu.cn; www.springer.com/journal/11582
E-mail: jzus_a@zju.edu.cn

Research Article
https://doi.org/10.1631/jzus.A2600050

A weak fault feature diagnosis method for electric drive systems based on a multi-source feature fusion selection mechanism

Cong YUE✉, Jingwen KANG, Yonghao ZHAO, Ping CHENG

Logistics Engineering College, Shanghai Maritime University, Shanghai 201306, China

Abstract: Electric drive systems (EDS) feature high integration and strong nonlinearity, which renders weak fault identification a challenging task. Acoustic particle velocity signals employed for noncontact fault monitoring are prone to contamination by noise and redundant features. This contamination seriously interferes with weak fault extraction and reduces diagnostic stability. To overcome the limitations of conventional single or multiple feature selection strategies, this paper proposes an information entropy-based multisource feature fusion selection (IE-MSFS) method. The proposed method can effectively eliminate redundant information and enhance the characterization ability of weak fault features. Based on the EDS acoustic particle velocity signals collected in the laboratory, a comparative analysis with vibration signals is carried out on three typical weak fault types through machine-learning evaluation. The results verify that the CIR-PS scheme exhibits outstanding and stable weak fault recognition performance, with a diagnostic accuracy exceeding 95.2%. Further tests demonstrate that the established scheme has favorable robustness and generalization ability for EDS weak fault diagnosis.

Keywords: Particle Velocity Signal, Weak Fault Diagnosis, Multi-source Fusion Feature Selection Mechanism, Enhanced Feature Extraction

1 Introduction

Electric drive systems (EDS), as a pivotal mechanical component, play an indispensable role in critical fields, including aerospace and shipping, serving as the core power support for high precision and high reliability. With the rapid advancement of industrial development, increasingly stringent requirements are imposed on the reliability of EDSs (Husain et al. 2021). Rolling bearings operate continuously under high-speed, complex loading conditions. Early-stage faults often manifest as faint, low-amplitude disturbances (Nawfal Mustafa 2021), readily obscured by ambient noise and other interferences to greatly hinder fault classification and identification. Consequently, in-depth investigation of these subtle faults is pivotal to achieving accurate fault diagnosis.

Fault diagnosis techniques based on vibration signals have reached a relatively mature stage. Its core procedures include signal acquisition by sensors, denoising preprocessing and fault feature extraction, and fault classification and identification via machine learning algorithms. However, the application of such methods in electric drive systems is constrained. On the one hand, EDS possesses complex internal structures. On the other hand, vibration sensors need to be closely attached to equipment surfaces, leading to inconvenient installation and potential safety hazards (Kuntoğlu et al. 2021). To address these limitations, Yao et al. (2025) adopted noncontact acoustic signals, which can effectively capture fault information owing to their high sensitivity to fault characteristics. To further strengthen weak fault signatures in acoustic signals, Hou et al. (2022) proposed a sparsity-oriented adjusted multipoint optimal minimum entropy deconvolution method. On this basis, Liu et al. (2025) developed a CNN− temporal convolutional network model, which achieves reliable fault feature detection from acoustic signals under complex noise interference.

The aforementioned research effectively extracts bearing fault characteristics from acoustic signals. Nevertheless, these methods are still vulnerable to environmental noise, and traditional denoising strategies often fail to achieve satisfactory performance. This limitation is particularly prominent under the superposition of multiple noise sources (Yang et al.

✉ Cong YUE, yuecong234@163.com
Cong YUE, https://orcid.org/0000-0002-2532-7195

Received Jan. 23, 2026; Revision accepted May 25, 2026; Crosschecked

2019). Conventional filtering struggles to effectively separate these signals, posing challenges for subsequent feature extraction and identification (Long et al. 2021). Mitigating the impact of this issue, Meng et al. (2022) employed the kurtosis criterion to apply intrinsic mode function (IMF) filtering, which bridges the connection between the actual fault spectrum and theoretical fault characteristic frequencies. To improve the extraction accuracy of complex signaling components, Miao et al. (2023) designed an adaptive finite impulse response filter for decomposing different modes, and utilized correlated kurtosis to extract mechanical fault features. Targeting residual noise interference in complex working conditions, Chen et al. (2021) proposed an adaptive time varying morphological filtering method. This method eliminates irrelevant interference components with the aid of diagonal slice spectrum analysis.

As the complexity of acoustic signals increases, directly extracting a large number of features tends to introduce noise and redundant data, thereby reducing the accuracy and stability of diagnostic models. In the study of complex dynamic systems, issues related to stability, uncertainty and anti-interference performance have long been important topics (Manivannan et al. 2020). For this reason, reasonable feature selection and robust indicator evaluation have become essential steps to improve fault diagnosis performance. To address redundant feature interference, Lao et al. (2023) introduced an adaptive feature selection method to reduce redundant features, thereby enhancing the ability to distinguish similar feature samples within multiclassification models. Extending this adaptive strategy, Wang et al. (2021) established a multi-criteria mathematical model. It efficiently extracts diverse low-dimensional near-optimal fault feature subsets. Aiming to address the inherent limitation of single evaluation metrics, Wang et al. (2022) devised a weighted fusion indicator based on kurtosis and spectral negative entropy. This design overcomes the drawbacks of single indicators and follows the systematic analysis principles for complex systems (Jusup et al. 2022).

Traditional diagnostic methods are limited by poor adaptability, insufficient noise resistance, and low diagnostic accuracy (Raj et al. 2025; Zhao et al. 2025). Machine learning models can effectively overcome these limitations through their robust feature learning and pattern recognition capabilities, enabling precise fault identification and classification. Wang et al. (2024) utilized recurrence quantization analysis to construct a feature matrix characterizing fault modes and severity, employing Bayesian optimization to determine the optimal parameters for the SVM. Experiments confirm that the method is capable of effectively distinguishing fault modes and quantifying fault severity levels. Wan et al. (2021) developed an efficient rolling element bearing fault diagnosis method based on Spark and an improved random forest algorithm by eliminating the decision trees with low classification accuracy and prone to repeated voting from the original random forest. Targeting reliable feature extraction, Tang et al. (2024) proposed a trustworthy multiscale secondary attention-embedded CNN for bearing fault diagnosis, introducing a reliable multiscale learning strategy to achieve dependable fault identification.

Current research focuses on screening high dimensional feature sets following feature extraction, employing dimension reduction methods such as principal component analysis (PCA) (Odhiambo Omuya et al. 2021) or linear discriminant analysis (LDA) (Lu et al. 2025) to select effective features. Current methods can reduce feature dimensionality to a certain extent. However, these methods still have obvious limitations. Signal reconstruction inevitably mixes noise components with fault-related features. This process preserves many invalid features and increases the difficulty of subsequent feature extraction and fault identification. In practical applications, multiple signal processing procedures are needed, including signal decomposition, reconstruction and feature screening. Repeated processing operations may cause the loss of subtle fault information and further reduce diagnostic accuracy. Acoustic signals are highly susceptible to strong background noise, which easily masks weak fault characteristics. Affected by redundant feature interference, existing methods struggle to maintain stable robustness under such complex working conditions.

Challenges faced by existing methods. The present study proposes a feature selection method, namely the multisource feature fusion selection mechanism based on information entropy (IE-MSFS), which analyses IMFs to extract latent fault characteristics at different frequency scales. IE-MSFS was combined with composite multiscale reverse weighted permutation entropy (CMRWPE) and PSO-SVM to form a new fault diagnosis model, CIR-PS. In Section 2, the IE-MSFS and CMRWPE methods are elaborated in detail. In Section 3, the experimental setup is introduced, including the acquisition of acoustic and vibration signals and the test conditions for EDS bearing faults. In Section 4, the experimental results validate the diagnostic performance of the model. In Section 5, conclusions are summarized.

2 Theoretical methods

This section focuses on the development of CIR-PS, beginning with an exposition of the core principles and implementation steps of IE-MSFS. The theoretical framework of CMRWPE is subsequently outlined, culminating in a detailed description of the workflow for the proposed model.

2.1 IE-MSFS framework

The IE-MSFS uses complete ensemble empirical mode decomposition with adaptive noise (CEEMDAN) (Chen et al. 2021) for original signal decomposition. This effectively mitigates environmental noise interference. The interference targets the extraction of subtle fault features from signals. The final decomposition result and residual signals of CEEMDAN are defined as follows:

$$\begin{cases} v(t) = \sum_{m=1}^{M} i_m(t) + r_M(t) \\ r_M(t) = v(t) - \sum_{m=1}^{M} i_m(t) \end{cases} \tag{1}$$

where $v(t)$ denotes the original sequence of the signal, and represents the total number of IMF components obtained from the decomposition of M, $i_m(t)$ refers to the *m*-th IMF obtained by decomposition.

IE-MSFS identifies IMF components containing meaningful information, and employs information entropy to select optimal time-domain features, thereby overcoming the limitation of traditional feature selection methods that focus solely on the features themselves. It further incorporates the Pearson correlation coefficient (Gong et al. 2024) for evaluation. This approach quantifies the association between each component and the original signal.

The specific steps of IE-MSFS are as follows:

Step 1: The original data sequence be denoted as $v(t)$. After CEEMDAN decomposition, s IMF sequences are obtained, where the *k*-th IMF is denoted as I_k $(k = 1, 2, \cdots, n)$.

Step 2: For each IMF, six typical time-domain metrics ($T_{k,t}$) are calculated: mean, variance, standard deviation, kurtosis, skewness, and root mean square value. These are sorted in this sequence, yielding a total of 6*n $T_{k,t}$. The formula for $T_{k,t}$ is defined as:

$$T_{k,t} = \begin{cases} \frac{1}{N}\sum_{j=1}^{N} i_{k,j} \\ \frac{1}{N-1}\sum_{j=1}^{N} (i_{k,j} - T_{k,1})^2 \\ \sqrt{T_{k,2}} \\ \frac{1}{N}\sum_{j=1}^{N} (\frac{i_{k,j} - T_{k,1}}{T_{k,3}})^4 - 3 \\ \frac{1}{N}\sum_{j=1}^{N} (\frac{i_{k,j} - T_{k,1}}{T_{K,3}})^3 \\ \sqrt{\frac{1}{N}\sum_{j=1}^{N} i_{k,j}^2} \end{cases} \tag{2}$$
$$(t = 1, 2, ..., 6)$$

Step 3: Information entropy is utilized to evaluate the discrepancy between time-domain metrics and raw data, defined as follows:

$$E(H, T_{k,t}) = \left| H(\mathrm{Y}) + \sum_{k=1}^{n} p(T_{k,t}) \log p(T_{k,t}) \right| \tag{3}$$

where $H(\mathrm{Y})$ is the entropy of the original data information, p represents the probability distribution of the acquired data, and n signifies the number of intervals $(k = 1, 2, 3, \cdots, 8)$.

Step 4: Calculate the ρ_k between I_k and the original data. Assuming $\boldsymbol{I}_k = [i_{s_k}, ..., i_{e_k}]$, the formula for calculating the absolute value of ρ_k for the original data and the *k*-th IMF is as follows:

$$\rho_k = \left| \frac{\sum_{j=s_k}^{e_k} (y_j - \overline{Y})(i_{k,j} - \overline{I_k})}{\sqrt{\sum_{j=1}^{N} \left(y_j - \overline{Y}\right)^2} \cdot \sqrt{\sum_{j=s_k}^{e_k} \left(i_{k,j} - \overline{I_k}\right)^2}} \right| \tag{4}$$

where the local mean $\overline{Y_k}$ is:

$$\overline{Y_k} = \frac{1}{e_k - s_k + 1} \sum_{j=s_k}^{e_k} i_{k,j} \tag{5}$$

Step 5: IMF selection is performed based on the time-domain features and correlation coefficients obtained from Steps 3 and 4. Fig. 1 illustrates the basic schematic of the IE-MSFS method.

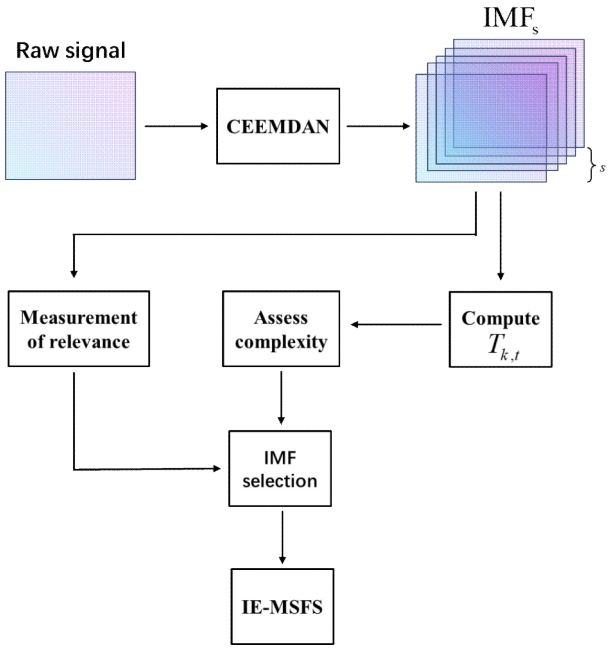

Fig. 1 Multisource Joint Feature Selection Mechanism based on Information entropy (IE-MSFS)

Fig. 1 illustrates the proposed multisource joint feature selection mechanism based on information entropy (IE-MSFS). The raw signal is decomposed into intrinsic mode functions by CEEMDAN. Each IMF is evaluated in two dimensions including relevance to the original signal and complexity based on computed entropy indicators. Optimal IMFs are selected to suppress noise and redundant components and form the feature set. This process aims to extract discriminative weak fault features and eliminate interference to improve the reliability of subsequent fault diagnosis.

2.2 Composite Multiscale Reverse Weighted Permutation Entropy

Reverse weighted permutation entropy (RWPE) (Gao et al. 2023) constitutes an enhanced algorithm derived from permutation entropy(PE). PE exhibits strong robustness to noise, but fails to account for amplitude variations between reconstruction sequences, resulting in shortcomings in impact amplitude analysis. RWPE addresses this deficiency by employing amplitude weighting and reverse weighting strategies, enabling the extraction of fault characteristics from complex raw data. The calculation formula for RWPE(E_{w}) is as follows:

$$E_{\mathrm{w}}\left(\mathrm{X}^{(m,t)}\right)=\sum_{r=1}^{m!}\left(P\left(\pi_r\right)-\frac{1}{m!}\right)^2 \tag{6}$$

where $P\left(\pi_r\right)$ denotes the probability of each arrangement.

Composite multiscale coarsening (CMSC) analysis overcomes the issue of neglecting subtle fault information inherent in multiscale coarsening (MSC) based on nonrepeating neighboring mean entropy calculations. This method precisely captures detailed temporal variations in signals, significantly enhancing the identification capability of fault characteristic information in nonlinear, nonstationary signals. The specific formula for composite multiscale coarsening is as follows:

$$Y_{a,b}^{s}=\frac{1}{a}\sum_{i=(j-1)a+b}^{ja+b-1}y_i \tag{7}$$
$$\left(a=1,2,3,\cdots,s,\ \ b=1,2,3,\cdots,a\right)$$

where s represents the maximum scale of coarse grained processing, y_i denotes the time series.

Fig. 2 shows the core differences between traditional multiscale coarsening (MSC) and composite multiscale coarsening (CMSC). The top row represents the original signal sequence, while the bottom rows depict the CMSC coarsening processes under different parameter settings. By introducing multiple window division patterns, CMSC effectively addresses the drawbacks of information loss and scale dependence in traditional MSC, generating more complete multiscale signal representations and providing a more stable and reliable data foundation for subsequent entropy analysis.

CMRWPE is constructed by combining composite multiscale coarsening with RWPE. By incorporating parallel subsequence calculations to compute average entropy values, it can fully extract hidden features within signals. The CMRWPE set calculation formula is defined below:

$$\mathrm{C}=\left\{E_{\mathrm{c}}\left(\mathrm{X}_{a,b}^{(m,i)}\right),i=1,2,3,\cdots,s\right\} \tag{8}$$

where C used to store all feature results from multiscale entropy analysis.

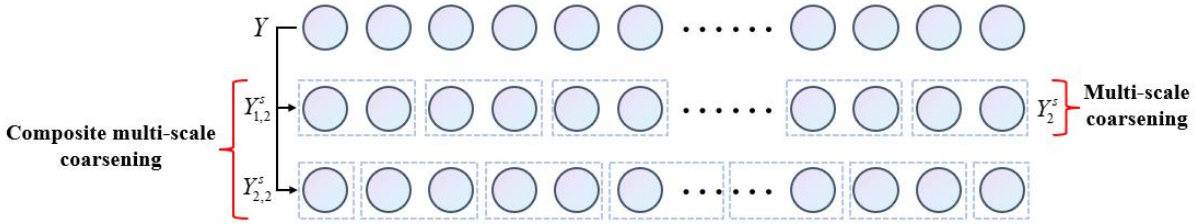

Fig. 2 Comparison of Principles Between MSC and CMSC

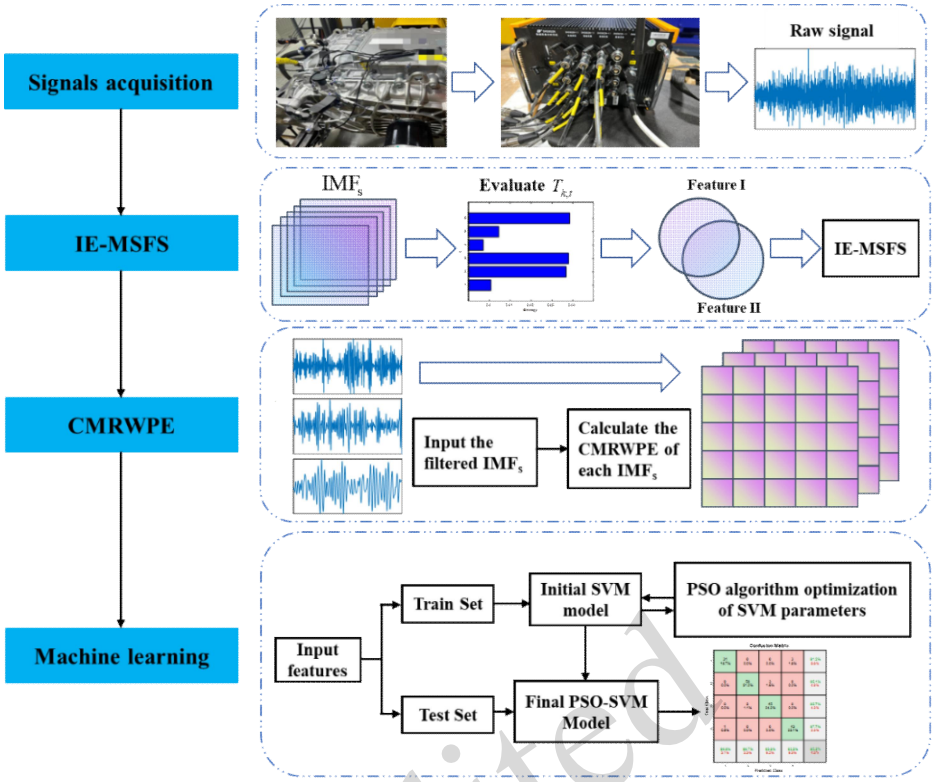

Fig. 3 Process flow of the CIR-PS Fault Diagnosis Model

2.3 Fault Diagnosis Framework CIR-PS

The flowchart of the proposed CIR-PS framework for the diagnosis of subtle faults in electric drive system bearings is shown in Fig. 3. This diagram illustrates the whole process ranging from signal collection to fault classification, and elaborates the cooperation of all functional modules.

The paper employs the PSO-SVM (Zhang et al. 2020). Particle swarm optimization (PSO) efficiently searches for the optimal parameters of SVM. It enhances the model capability to process complex data and reduces noise interference.

The specific steps of the CIR-PS fault diagnosis model are as follows:

(1) Acoustic signals were collected via sensors.

(2) The captured acoustic signals are decomposed using the CEEMDAN method to obtain multiple IMFs, thereby reducing noise interference;

(3) Employ IE-MSFS for filtering, retaining IMFs containing effective feature information to enhance fault feature extraction capability.

(4) Calculate feature entropy values for the filtered IMFs using CMRWPE to uncover subtle fault characteristics.

(5) Utilize PSO-SVM to identify subtle faults in the electric drive system based on the obtained feature entropy values.

3 Experimental study

The validity and stability of the proposed method were verified through bench testing conducted in our EDS testing laboratory (Yue et al. 2024). The EDS, as depicted in Fig. 4, constitutes a critical component of the test system. It serves as the core data acquisition unit, responsible for collecting raw signals under different working conditions for subsequent fault diagnosis analysis. All tests strictly adhered to standardized operating conditions, with a constant rotational speed of 1000 rpm and a constant torque of 50 Nm. Each single condition measurement lasted no less than 120 seconds and was paired with a 20 kHZ sampling frequency to ensure sufficient cyclic samples. A particle velocity sensor (PVS) was mounted on a customized bracket external to the EDS to capture the acoustic particle velocity signal. This signal can directly quantify vibration states, offering advantages in identifying weak fault information. Integrated Electronics Piezo Electric (IEPE) and Micro-Electro Mechanical System (MEMS) sensors were employed to acquire dynamic signals, with key sensor parameters referenced from Ref. (Yue et al. 2025).

Rolling bearings of model NSK-6307 were employed to design faults, considering four health states: rolling element fault (REF), outer ring fault (ORF), inner ring fault (IRF), and normal state (NOR).

This study employs artificially designed micro faults (both the fault depth and width are relatively small) to simulate the characteristic patterns of early-stage, subtle faults in equipment. Detailed information regarding the bearing fault design is presented in Table 1.

Figs. 5 and 6 present time-domain waveforms and frequency spectra of acoustic particle velocity signals, respectively, along with time-domain curves of vibration signals collected by IEPE and MEMS sensors. Four typical bearing states are studied, including the normal state, outer race fault and inner race fault. The acoustic signal exhibits chaotic and irregular fluctuations in the time domain while its fault-related spectral components are widely distributed and scattered across the frequency axis. Its fault related frequency components are widely dispersed. These features mask valid fault information and obscure characteristic fault frequencies, thus hindering direct fault diagnosis based on original signals.

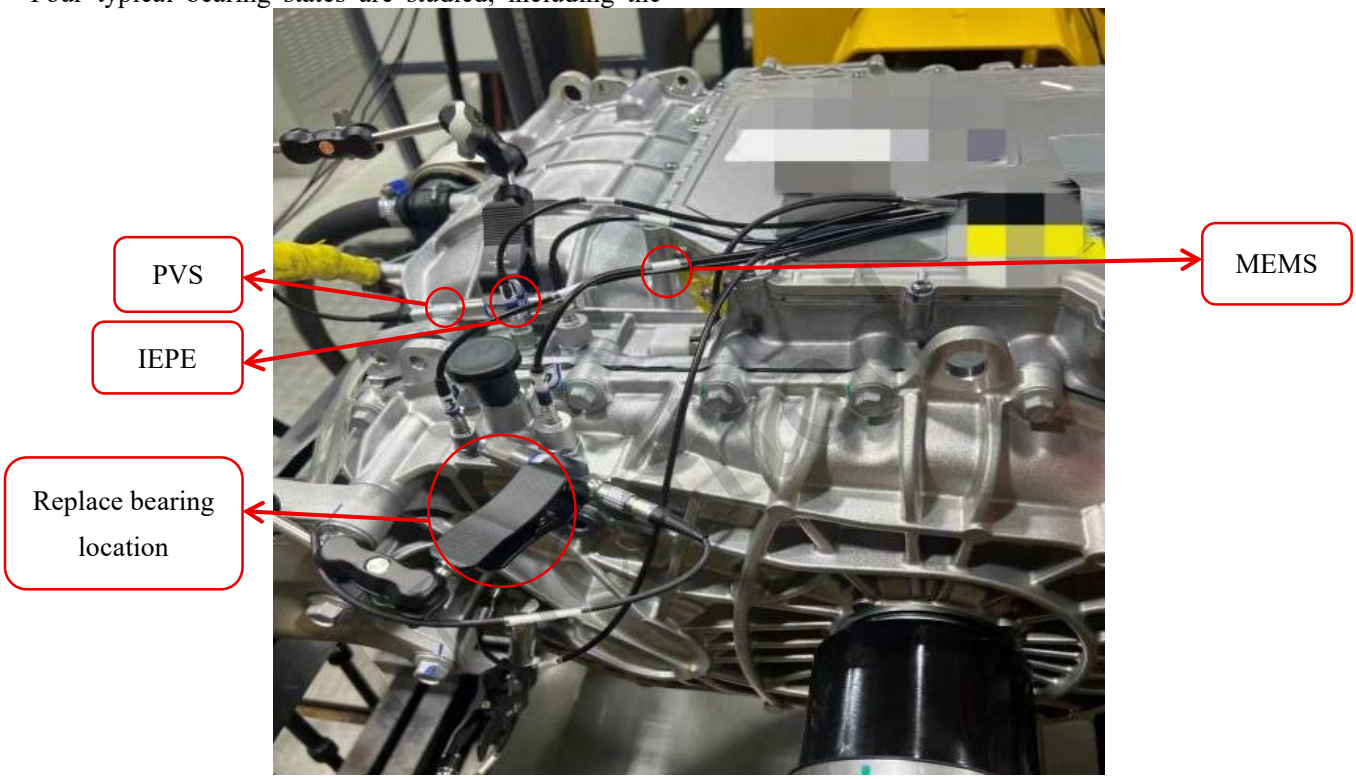

Fig. 4 EDS experimental bench

Table 1 Rolling bearing fault setting

Fault Type	Fault width	Fault depth	Abbreviation	Label
Rolling element fault	approx. 3 mm	approx. 1 mm	REF	1
Outer ring failure	approx. 0.6 mm	approx. 1 mm	ORF	2
Inner ring failure	approx. 0.6 mm	approx. 1 mm	IRF	3
Normal bearing	no defect	no defect	NOR	4

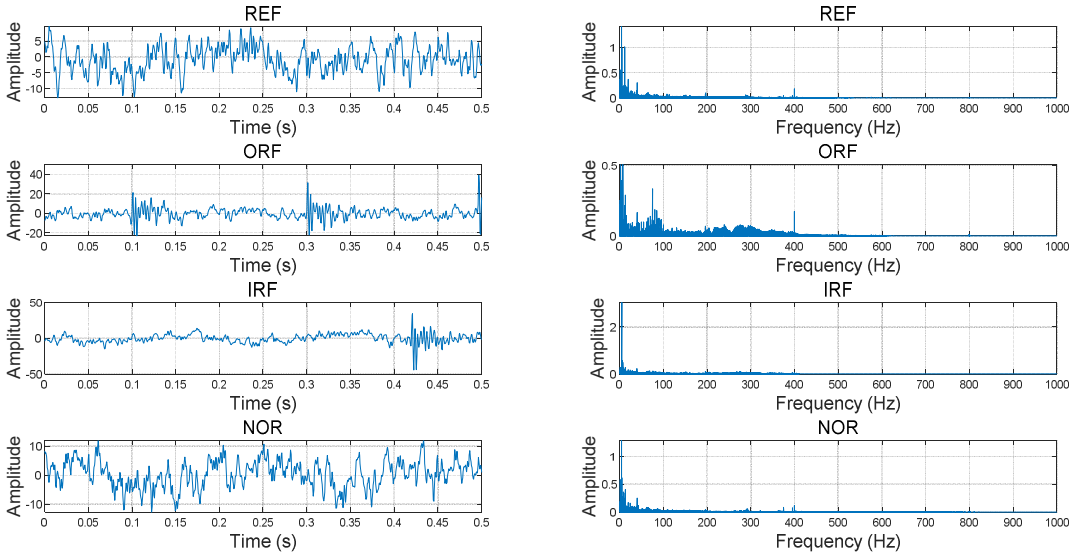

Fig. 5 Acoustic particle velocity signal time-domain plot and frequency spectrum

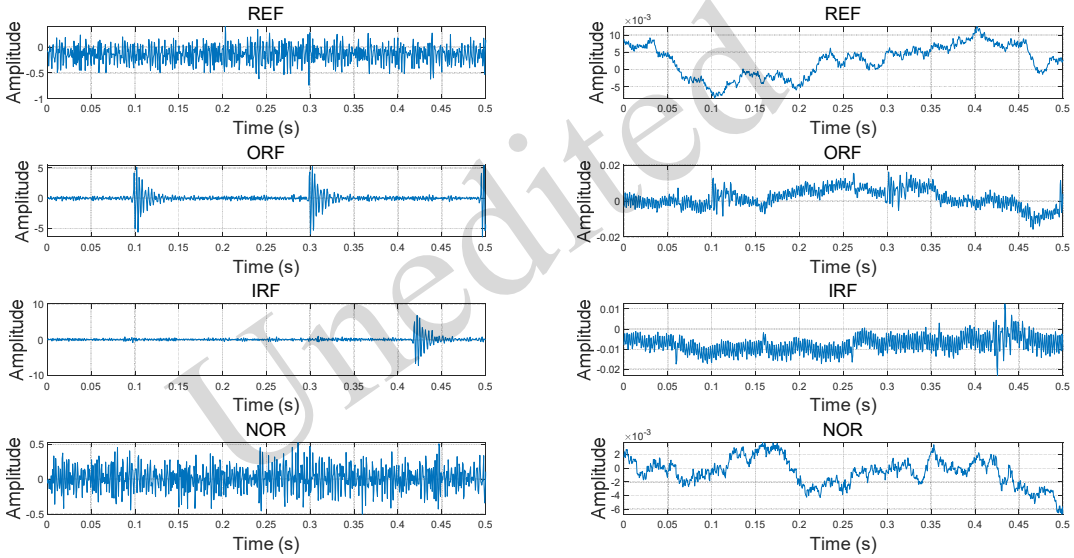

Fig. 6 Time-domain plots of vibration signals from IEPE sensors and MEMS sensors

To further analyze the fault signal and identify its intrinsic components, the CEEMDAN method was employed to decompose a rolling element fault signal. The spectra of the resulting IMFs are shown in Fig. 7. This step aims to isolate the frequency components associated with the fault from those dominated by noise or driven by trends, thereby enabling an analysis of how different IMFs carry distinct fault information.

After CEEMDAN as shown in Fig. 7, diverse IMF components are acquired with distinct spectral characteristics. High-order components from IMF6 to IMF10 are mainly distributed below 500 Hz and gather energy near the direct current, which reflects low-frequency trends and background noise. By comparison, low-order components from IMF1 to IMF5 cover the frequency range of 0 to 4000 Hz and contain major bearing fault frequency bands. Among them, IMF1 to IMF3 carry sufficient medium- and high-frequency information, and IMF4 to IMF5 concentrate energy in medium- and low-frequency bands, matching the theoretical fault characteristic frequencies well. The above results prove that the selected IMFs can fully extract valid fault information and verify the rationality of the screening strategy based on kurtosis and the correlation coefficient.

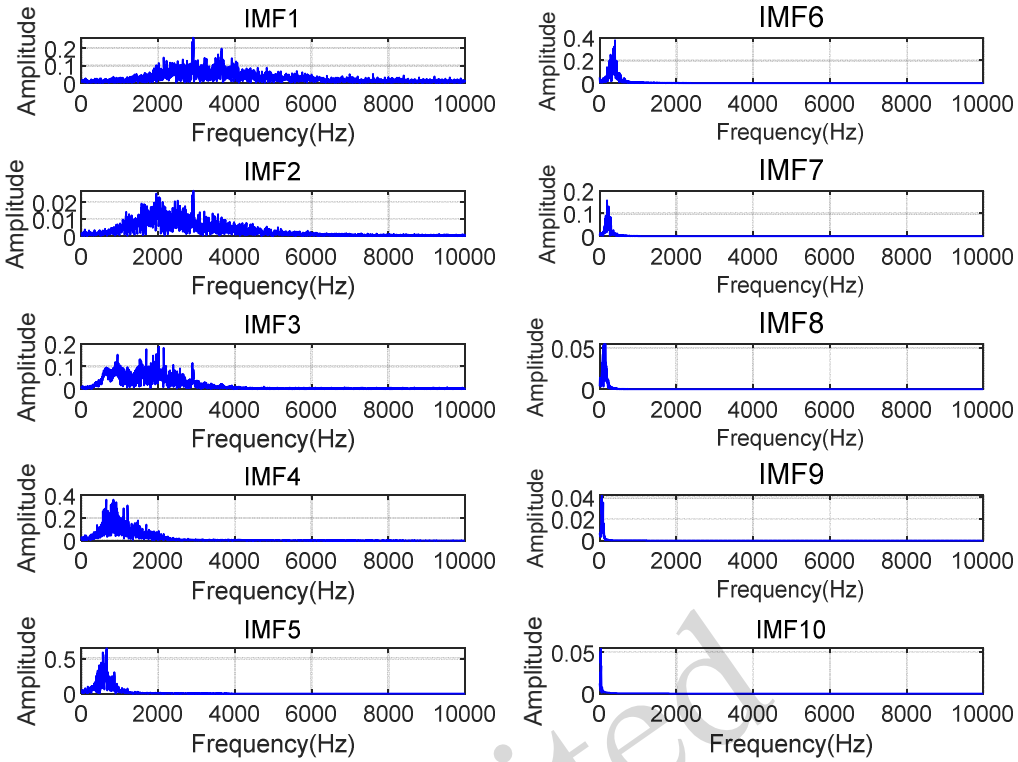

Fig. 7 IMF spectrogram based on CEEMDAN

4 Comparative analysis

The acoustic particle velocity signal serves as the research target, and the IE-MSFS parameters were determined. Signal-to-noise ratio tests and ablation experiments verified the feature extraction stability and CIR-PS module contributions. A model accuracy comparison was conducted to characterize the fault detection ability of various algorithms under different signal quality scenarios.

4.1 IE-MSFS Parameter Analysis

Random sampling of the weak fault acoustic particle velocity signal was conducted, followed by IE-MSFS analysis. CEEMDAN decomposition yielded twelve IMF components. A 12×6 matrix was constructed based on $T_{k,t}$, integrating information entropy quantification features with indicator importance.

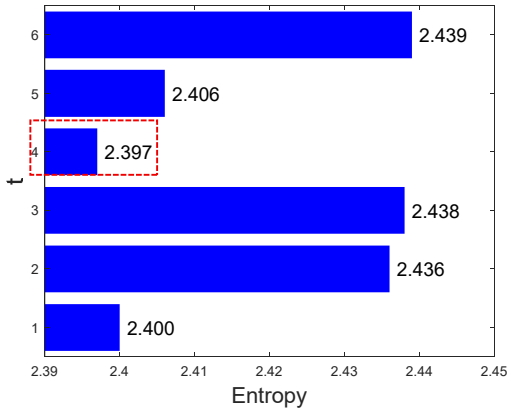

Fig. 8 Horizontal bar chart of time-domain indicator information entropy values

The horizontal bar chart in Fig. 8 shows the entropy values of six different time-domain features calculated by the proposed method, revealing that the entropy value is minimal at t=4 (as indicated by the red dashed box), with the corresponding kurtosis more effectively reflecting fault characteristics. As kurtosis is constrained by time-domain analysis, the Pearson correlation coefficient is introduced to assist in screening.

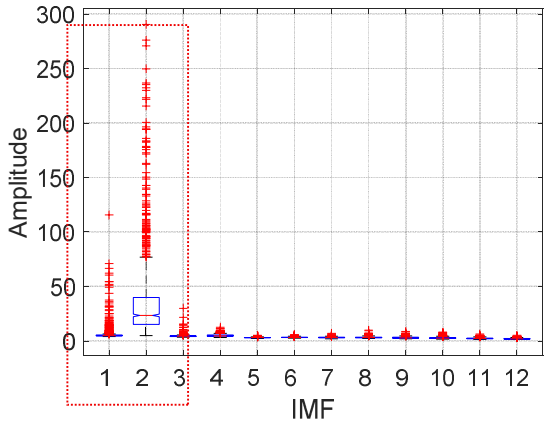

(a) Kurtosis

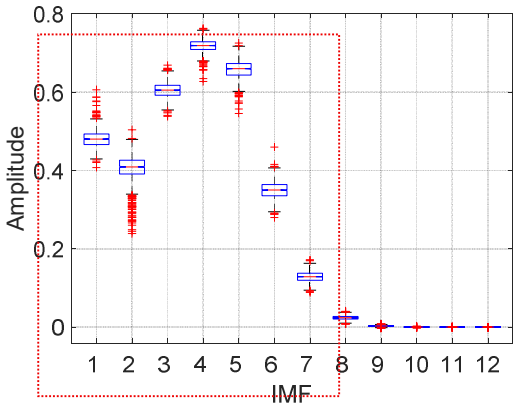

(b) Correlation Coefficient

Fig. 9 Acoustic particle velocity signal box diagram

Fig. 9 quantifies the stability of IMFs through the distribution of kurtosis and correlation coefficients. In Fig. 9a, outliers in IMF2 indicate intermittent impacts and persistent wear. In Fig. 9b, high-frequency components IMF1-7 contain fault information, especially IMF4. Based on these results, IMF3 is selected to ensure the reliability of subsequent analysis.

The preliminary IMF parameter *n* is set to 3, where *n* denotes the IMF order. The diagnostic accuracy of weak faults is analyzed under different values of *n*. All experiments were repeated five times to minimize random variation. The minimum accuracy, mean accuracy, and average processing time are shown in Tables 2 and 3.

Table 2 indicates that the average diagnostic accuracy for inner and outer ring faults (Categories 2 and 3) across all parameter types reached approximately 96%. Only when *n*=3 did the diagnostic performance for rolling element faults versus normal conditions (Categories 1 and 4) demonstrate superiority.

Table 2 Fault diagnosis accuracy of different *n* (%)

	REF			ORF			IRF			NOR		
n	max	min	mean	max	min	mean	max	min	mean	max	min	mean
1	95.1	80.2	88.5	97.1	74.8	90.4	99.5	97.6	98.8	100	95.3	97.6
2	94.1	90.1	92.3	96.4	93.8	95.4	98.0	95.9	96.6	96.0	90.3	93.1
3	95.7	92.2	94.6	99.7	92.7	96.1	100	93.2	96.3	100	96.1	98.0
4	92.6	84.9	89.9	96.2	95.1	95.6	99.2	94.5	97.6	97.2	93.8	94.9
5	91.3	82.6	87.5	98.3	90.2	95.2	99.2	95.0	97.9	95.9	82.7	88.6
6	92.2	82.9	86.9	99.2	95.2	96.5	99.1	95.3	97.1	93.0	89.7	92.4
7	86.5	81.2	84.6	98.4	96.7	97.5	99.2	96.6	97.5	91.7	86.8	88.5
8	87	80.0	84.5	99.1	96.2	97.3	99.2	97.4	98.3	90.2	80.5	84.5

Table 3 Mean accuracy rates and processing times of different *n*

n	1	2	3	4	5	6	7	8
Accuracy	93.1%	93.4%	95.7%	94.2%	92.5%	92.4%	91.9%	90.1%
Time	27.9 s	29.6 s	30.2 s	38.8 s	42.1 s	43.6 s	43.5 s	43.9 s

Table 3 shows that with the increment of the parameter n, the diagnostic accuracy initially rises before declining, while the computation time progressively increases. When *n*=3, the utilization of effective feature information reaches an optimum, achieving a peak diagnostic accuracy of 95.7%. Beyond *n*=3, the introduction of redundant feature information interferes with the extraction of effective features, ultimately leading to a decline in performance. Balancing accuracy and computational cost, *n*=3 is determined as the optimal parameter. The proposed CIR-PS model screens effective IMFs to suppress interference caused by redundant features. This approach significantly enhances the representation capability of weak fault features.

4.2 Signal-to-Noise Ratio Experimental Analysis

To validate the performance of IE-MSFS in improving the feature extraction stability of acoustic signals, the entropy values from the CIR (IE-MSFS coupled with CMRWPE) and CMRWPE methods are compared at multiple scales. Comparative analysis is conducted under SNR levels of 5, 10, 15, and 20 dB, where different noise environments are constructed by injecting Gaussian white noise into the original signal.

To verify the noise robustness of the proposed feature extraction method, the comparison results of CMRWPE and CIR under different signal-to-noise ratios are presented in Fig. 10.

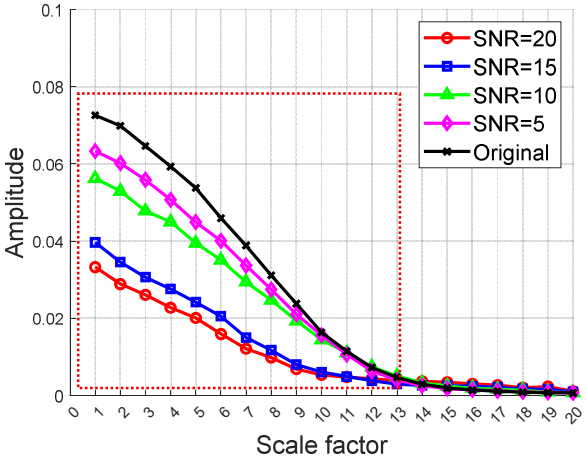

(a) CIR

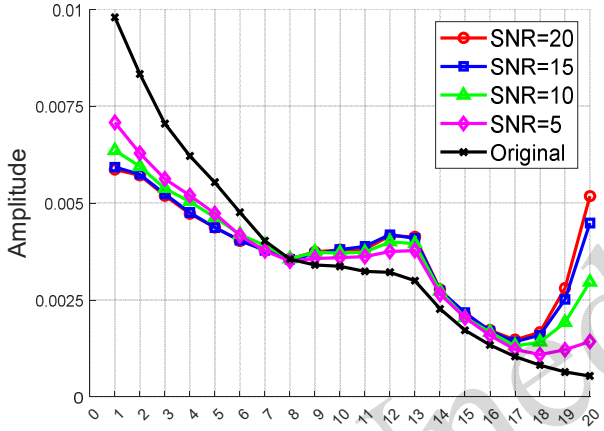

(b) CMRWPE

Fig. 10 Entropy results for acoustic particle velocity signal under signal-to-noise ratio conditions

As shown in Fig. 10, there is a significant disparity in the entropy values obtained by the two methods. The CMRWPE curves exhibit relatively stable variation across scales, whereas the CIR curves show a gradual decline with clear divergence at low scales. Between scales 9 and 13, the CIR values progressively approximate the original signal. When the scales exceed 14, the curves for different SNRs converge. This indicates that beyond a specific scale threshold, CIR enables stable feature extraction and exhibits robust anti-noise performance.

To evaluate the anti-noise robustness of the proposed method CIR and the competing approach CMRWPE for weak fault diagnosis, their diagnostic accuracies obtained via the SVM classifier are compared across SNRs ranging from 0 to 20 dB.

As shown in Fig.11, CMRWPE exhibits superior performance under low SNR conditions (0–10 dB), maintaining a stable accuracy above 60% and peaking at 73.5%, which highlights its strong robustness against heavy background noise. In contrast, CIR starts at a lower accuracy of 43% at 0 dB but shows a steady improvement with increasing SNR, eventually surpassing CMRWPE at 15 dB and reaching 74.5% at 20 dB. The core finding is that CMRWPE is more suitable for strong-noise environments, while SNR demonstrates better performance as the signal quality improves.

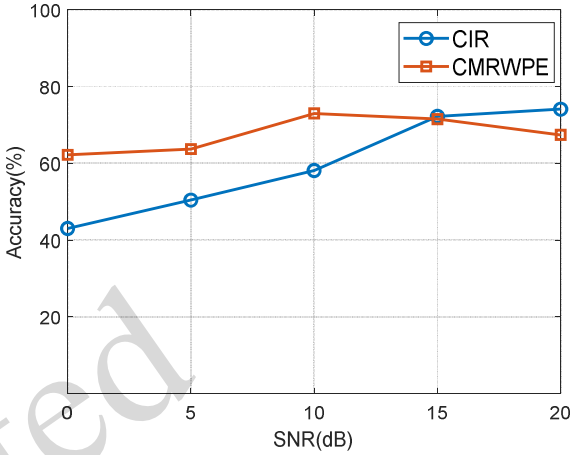

Fig. 11 Accuracy comparison in different SNR levels

4.3 Ablation Experiment

Ablation experiments quantitatively assess the efficacy of each module in the CIR-PS model (A9) for acoustic particle velocity signal diagnosis. We use the traditional model (A10) as the reference. It applies VMD to process raw signals, leverages PE to capture fault features, and finally uses SVM to complete fault identification. Within this framework, ablation models are constructed by progressively replacing individual modules of the A9 model with their counterparts from the A10 model, as detailed in Table 4. The symbol '√' denotes the adoption of the baseline A9 model method for the corresponding module.

In ablation experiments, the F1-score (Naidu et al. 2023) is employed as an evaluation metric to assess model reliability. This indicator represents the harmonic mean of precision and recall, defined as follows:

$$F_1 = 2 \times \frac{P \cdot R}{P + R} \begin{cases} P = \dfrac{N_{TP}}{N_{TP} + N_{FP}} \\ R = \dfrac{N_{TP}}{N_{TP} + N_{FN}} \end{cases} \tag{9}$$

where P and R stand for precision and recall respectively, N_{TP} denotes correctly identified faulty samples, N_{FP} denotes misdiagnosed normal samples, and N_{FN} denotes missed faulty samples.

Table 4 Experimental settings for each generalization task in the ablation experiment

Model	Module			
	Signal decomposition (a)	Feature selection (b)	Feature (c)	Machine (d)
A1		√	√	√
A2	√		√	√
A3	√	√		√
A4	√	√	√	
A5			√	√
A6		√	√	
A7	√			√
A8		√		√
A9	√	√	√	√
A10				

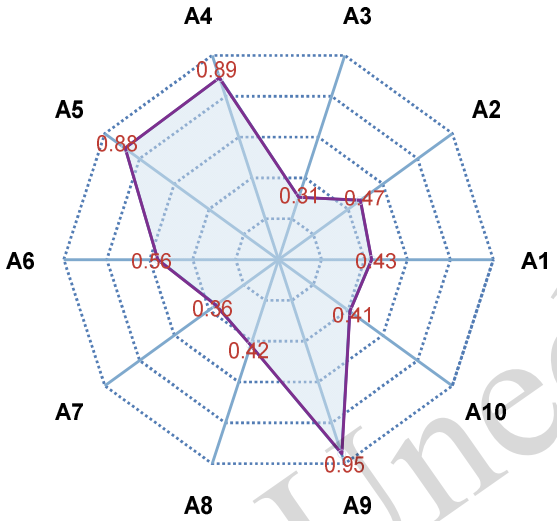

Fig. 12 Fault diagnosis results in terms of F1-score (%)

The ablation experiment results in Fig. 12 demonstrate the importance of each module in the proposed method for weak fault diagnosis. Removing any key module leads to a significant drop in the F1-score, exceeding 0.4 in some cases. The dual-module ablation further reveals synergistic and compensatory effects between modules, with some components showing strong dependencies on others. Overall, the results confirm that the collaborative optimization of all modules is critical to maintaining stable performance and high diagnostic accuracy.

4.4 Machine learning analysis

To validate the impact of machine learning on CIR performance, BP, SVM, ELM, PLS, PSO-BP, and PSO-SVM were selected for comparison. BP exhibits strong fitting capability, SVM demonstrates superior generalization and noise robustness, PLS adapts well to high-dimensional features, ELM offers rapid training speed, and methods based on PSO enhance performance through parameter adjustment.

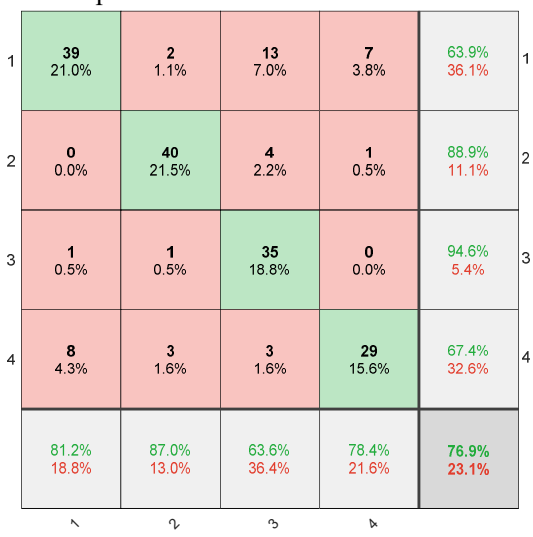

(a) BP

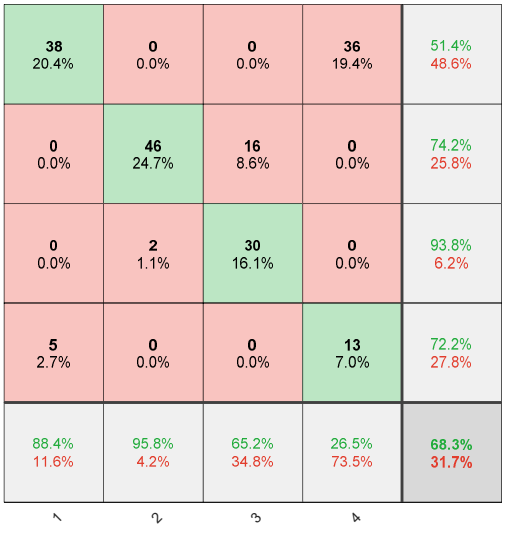

(b) SVM

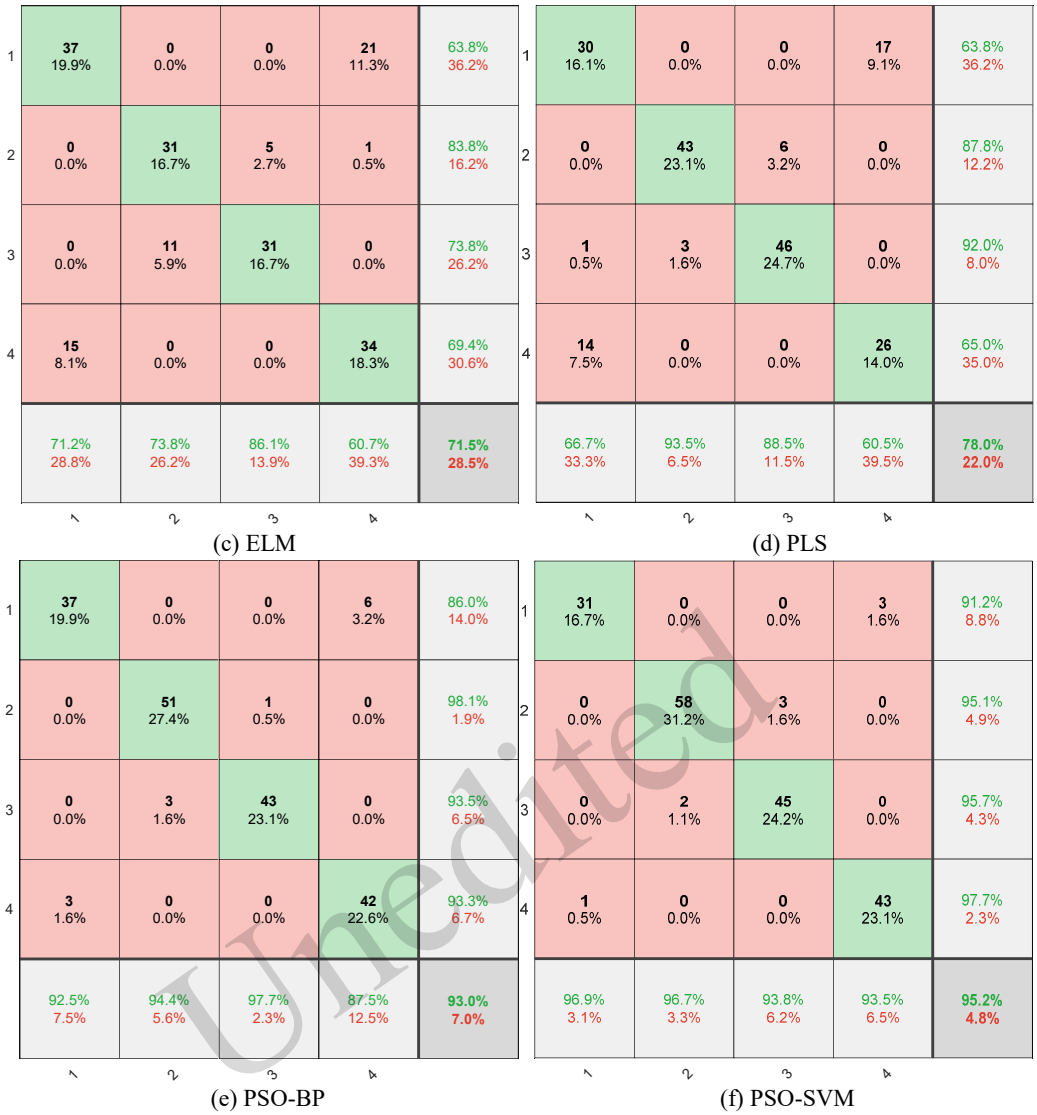

Fig. 13 Machine Learning Comparison

The confusion matrices of six machine learning classifiers are presented in Fig. 13, showing their performance on the acoustic particle velocity signal fault classification task. The SVM achieves the lowest accuracy of 68.3%, while both PSO-BP and PSO-SVM exceed 93%, confirming that PSO-SVM is highly effective for subtle fault identification.

To comprehensively evaluate the effectiveness of the proposed method, six machine learning models are compared across accuracy, F1-score, and recall metrics, as shown in Fig. 14.

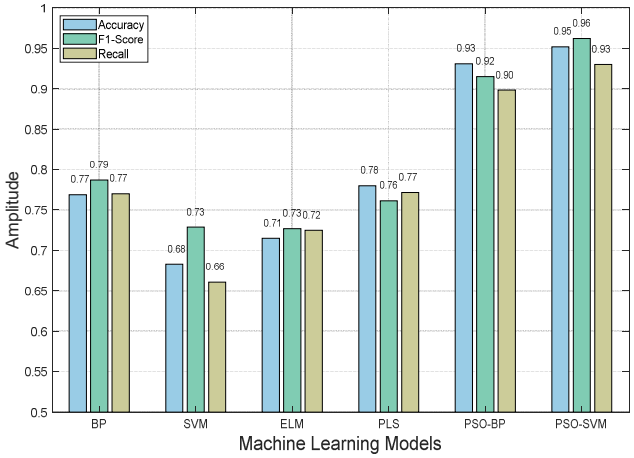

Fig. 14 Performance Comparison Chart of Machine Learning Models

As shown in the bar chart in Fig. 14, this illustrates a comparison of the performance of six machine learning models across three key metrics. The results

show that PSO-SVM achieves the highest and most balanced performance across all three metrics, outperforming other models and demonstrating its effectiveness in reducing both misdiagnosis and missed diagnosis.

4.5 Comparison of acoustic and vibration signals

The generalization capability of the CIR-PS model was validated based on IEPE and MEMS vibration signals. Calculate parameter $T_{k,t}$ separately for each individual vibration signal, determine t=4 for the MEMS signal and t=3 for the IEPE signal. The box plot shows the distributions of different metrics for MEMS and IEPE signals, aiming to determine the optimal performance indicator, as shown in Fig. 15.

From the results presented in Fig. 15, the high-frequency components of the IEPE vibration signal are concentrated in the range of 1–4; thus, the upper limit is set to 4, the MEMS vibration signal shows high-frequency components covering 1–3, and the corresponding upper limit is determined as 3. Features are extracted from the screened IMFs, and the obtained feature set is input into the PSO-SVM for fault classification and identification The machine learning classification results are presented in Figs. 16, 17 and 18. These visualizations quantify label consistency and classwise classification performance and reveal fault identification accuracy and misclassification patterns.

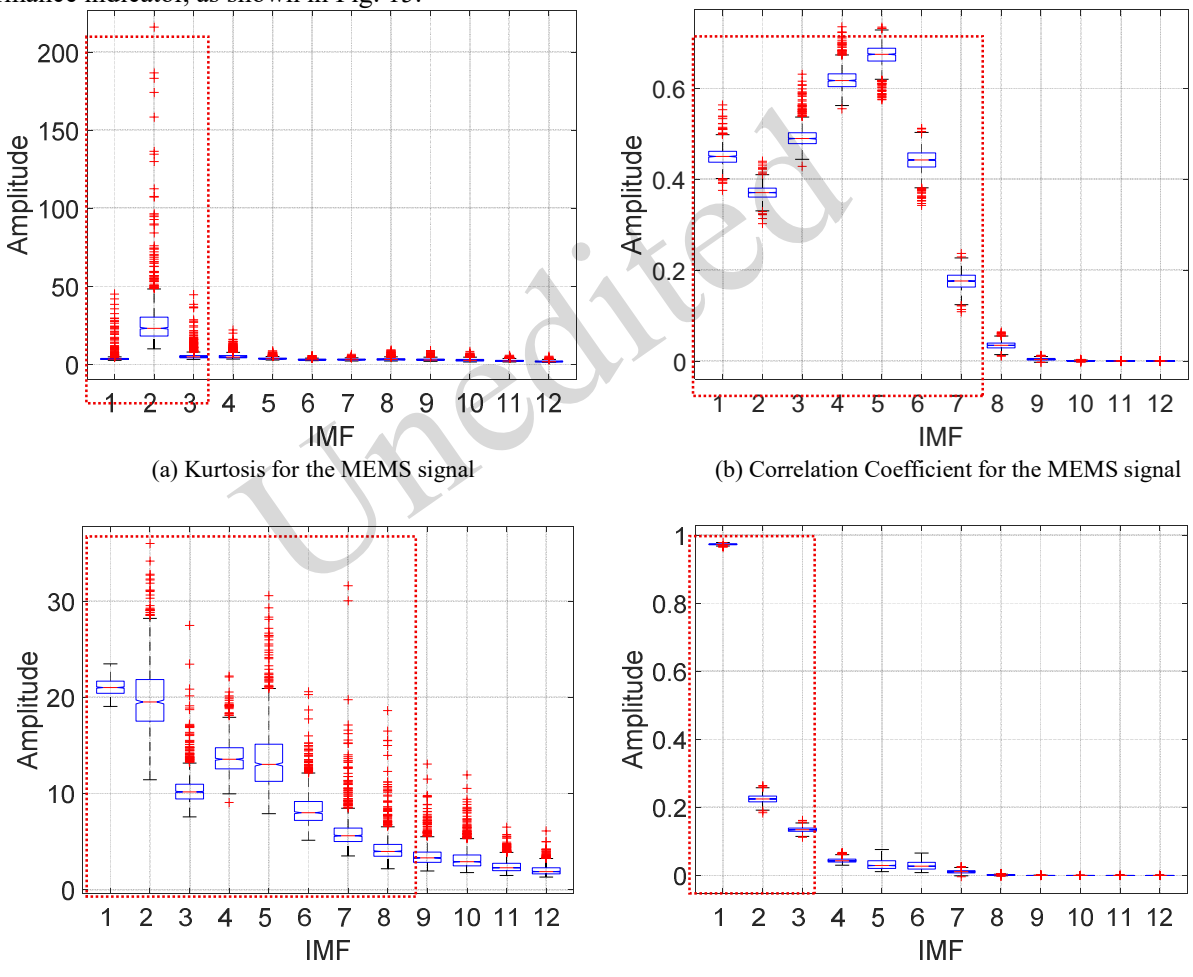

(a) Kurtosis for the MEMS signal

(b) Correlation Coefficient for the MEMS signal

(c) Standard deviation for the IEPE signal

(d) Correlation coefficient for the IEPE signal

Fig. 15 Box diagrams of the MEMS signal and IEPE signal under different metrics

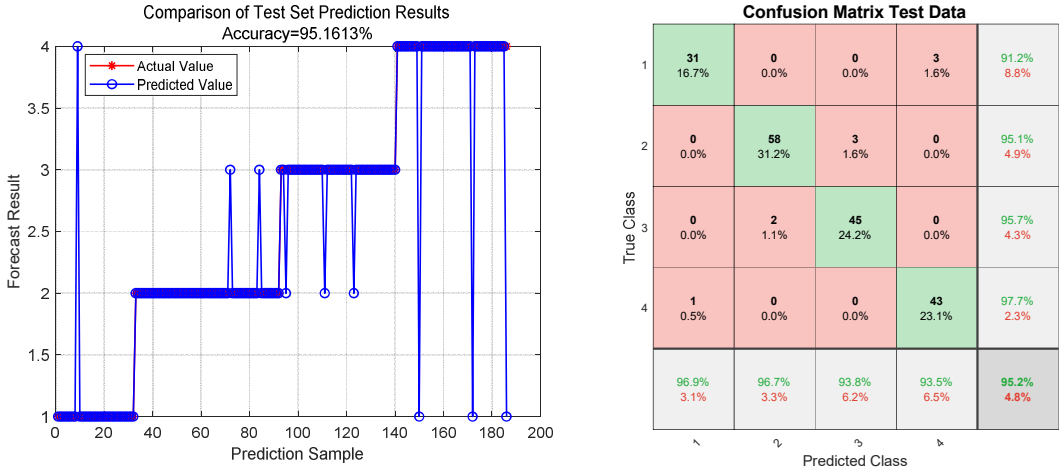

Fig. 16 Machine Learning of the Acoustic Particle Velocity Signal

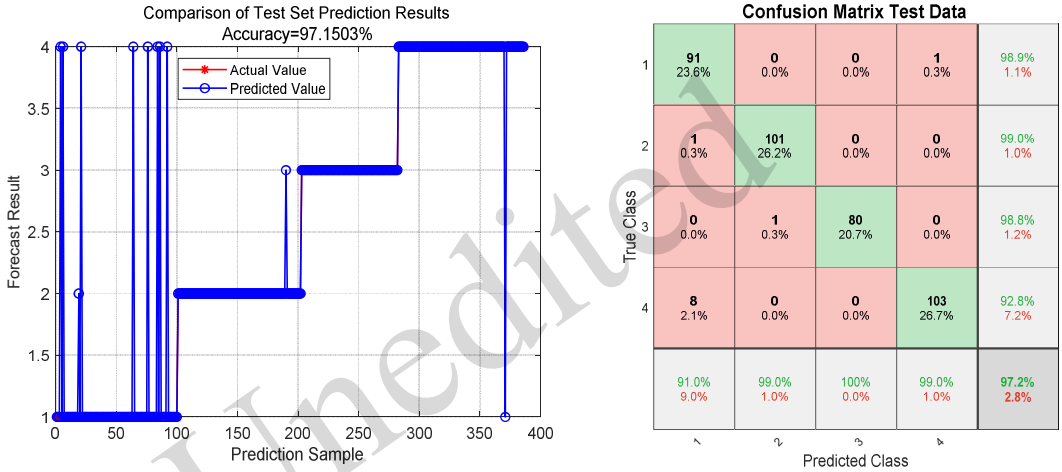

Fig. 17 Machine Learning of High-Quality Vibration Signals

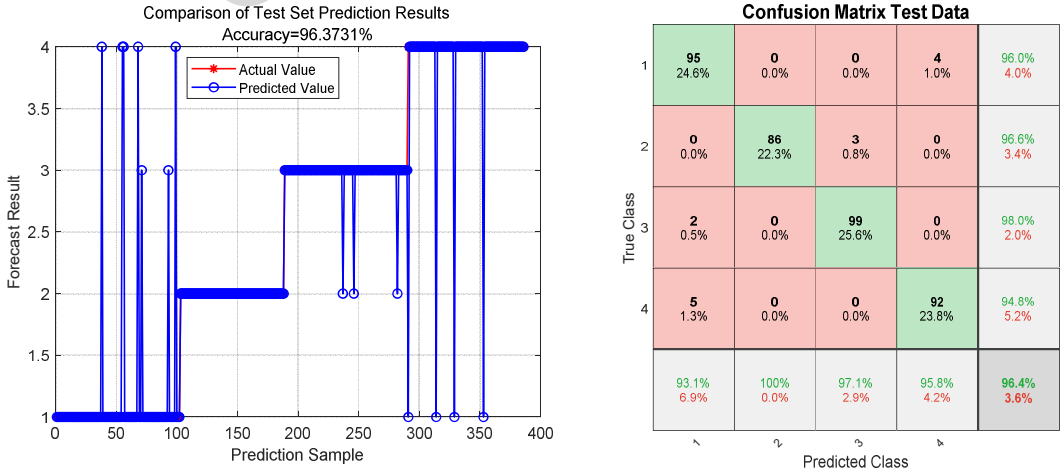

Fig. 18 Machine Learning of Low-Quality Vibration Signals

The results indicate that the CIR-PS delivers high recognition accuracy in acoustic particle velocity signals while maintaining favorable precision in the diagnosis of MEMS and IEPE signals. The diagnostic accuracy for all three signal types exceeded 95%, confirming that CIR-PS possesses generalizability across different signal types.

5 Conclusions

This study focuses on the accurate and efficient diagnosis of subtle bearing weak faults in EDS. Based on acoustic and vibration signal data acquired from a laboratory EDS test bench, the overall research

conclusions are follows:

(1) A novel feature selection method, namely, the IE-MSFS method, is proposed to tackle the issues of noise interference and redundancy in weak fault diagnosis. It employs multi–indicator screening of IMF components to suppress redundant features and enhance the representation of weak fault features under noisy conditions.

(2) Based on the proposed IE-MSFS method, the CIR-PS model is validated using three typical EDS weak fault acoustic signals. Experimental results under different SNR confirm its excellent anti-noise robustness, with diagnostic accuracy higher than 95.2%.

(3) Validations on two vibration signal datasets show that the CIR-PS model can effectively distinguish inner and outer race weak faults. It achieves a minimum accuracy of 96.4%, demonstrating good generalization and practicability.

The present study identifies acoustic signals for subtle bearing faults in the EDS to facilitate noncontact diagnosis. Although utilizing acoustic and vibration data is effective for single weak faults under stable laboratory conditions, it fails to address compound faults or time-varying operating conditions. Future research will focus on the detection and validation of compound weak faults under variable conditions to support practical engineering applications.

Acknowledgements

The authors would like to express their gratitude to NIO for fruitful discussions on topics relevant to this work. This research was supported by the National Natural Science Youth Foundation of China (52301328). Finally, the authors express sincere appreciation to all reviewers for their valuable comments.

Author contributions

Cong Yue and Jingwen Kang designed the research. Jingwen Kang and Yonghao Zhao processed the corresponding data. Jingwen Kang wrote the first draft of the manuscript. Cong Yue and Ping Cheng helped to organize the manuscript. Cong Yue and Jingwen Kang revised and edited the final version.

Conflicts of interest statement

The authors declare that we have no competing financial interests or personal relationships that could have appeared to influence the work reported in preparing this article.

Data availability

The data that support the findings of this study are available from the corresponding author upon reasonable request.

References

Chen B, Song D, Zhang W, et al., 2021. A performance enhanced time-varying morphological filtering method for bearing fault diagnosis. *Measurement,* 176: 109163. https://doi.org/10.1016/j.measurement.2021.109163.

Chen W, Li J, Wang Q, et al., 2021. Fault feature extraction and diagnosis of rolling bearings based on wavelet thresholding denoising with CEEMDAN energy entropy and PSO-LSSVM. *Measurement,* 172: 108901. https://doi.org/10.1016/j.measurement.2020.108901.

Gao H, Wu C, Zhu D, et al., 2023. Feature Extraction Method of Underwater Acoustic Signals Using VMD and Reverse Weighted Permutation Entropy. In *2023 6th International Conference on Information Communication and Signal Processing (ICICSP),* 465–470. https://doi.org/10.1109/ICICSP59554.2023.10390552.

Gong H, Li Y, Zhang J, et al., 2024. A new filter feature selection algorithm for classification task by ensembling pearson correlation coefficient and mutual information. *Engineering Applications of Artificial Intelligence,* 131: 107865. https://doi.org/10.1016/j.engappai.2024.107865.

Hou Y, Zhou C, Tian C, et al., 2022. Acoustic feature enhancement in rolling bearing fault diagnosis using sparsity-oriented multipoint optimal minimum entropy deconvolution adjusted method. *Applied Acoustics,* 201: 109105. https://doi.org/10.1016/j.apacoust.2022.109105.

Husain I, Ozpineci B, Islam MS, et al., 2021. Electric Drive Technology Trends, Challenges, and Opportunities for Future Electric Vehicles. *Proceedings of the IEEE,* 109: 1039–1059. https://doi.org/10.1109/JPROC.2020.3046112.

Jusup M, Holme P, Kanazawa K, et al., 2022. Social physics. *Physics Reports,* 948: 1–148. https://doi.org/10.1016/j.physrep.2021.10.005.

Kuntoğlu M, Salur E, Gupta MK, et al., 2021. A state-of-the-art review on sensors and signal processing systems in mechanical machining processes. *The International Journal of Advanced Manufacturing Technology,* 116: 2711–2735. https://doi.org/10.1007/s00170-021-07425-4.

Lao Z, He D, Wei Z, et al., 2023. Intelligent fault diagnosis for rail transit switch machine based on adaptive feature selection and improved LightGBM. *Engineering Failure Analysis,* 148: 107219. https://doi.org/10.1016/j.engfailanal.2023.107219.

Liu Y, Xu Z, He Y, et al., 2025. Acoustic fault diagnosis method for rotating machinery based on improved spectral subtraction and CNN-TCN model. *Measurement,* 256: 118482. https://doi.org/10.1016/j.measurement.2025.118482.

Long J, Wang X, Zhou W, et al., 2021. A Comprehensive Review of Signal Processing and Machine Learning Technologies for UHF PD Detection and Diagnosis (I): Preprocessing and Localization Approaches. *IEEE Access,* 9: 69876–69904. https://doi.org/10.1109/ACCESS.2021.3077483.

Lu N, Li Z, Liu D, et al., 2025. A feature extraction method for rotating machinery fault diagnosis based on a multiscale entropy fusion strategy and GA-RL-LDA model. *Soft Computing,* 29: 1747–1765. https://doi.org/10.1007/s00500-025-10484-4.

Manivannan R, Samidurai R, Cao J, et al., 2020. Design of Resilient Reliable Dissipativity Control for Systems With Actuator Faults and Probabilistic Time-Delay Signals via Sampled-Data Approach. *IEEE Transactions on Systems,*

Man, and Cybernetics: Systems, 50: 4243–4255. https://doi.org/10.1109/TSMC.2018.2846645.

Meng D, Wang H, Yang S, et al., 2022. Fault Analysis of Wind Power Rolling Bearing Based on EMD Feature Extraction. *Computer Modeling in Engineering & Sciences,* 130: 543–558. https://doi.org/10.32604/cmes.2022.018123.

Miao Y, Zhang B, Li C, et al., 2023. Feature Mode Decomposition: New Decomposition Theory for Rotating Machinery Fault Diagnosis. *IEEE Transactions on Industrial Electronics,* 70: 1949–1960. https://doi.org/10.1109/TIE.2022.3156156.

Naidu G, Zuva T, Sibanda EM, 2023. A Review of Evaluation Metrics in Machine Learning Algorithms. In *Artificial Intelligence Application in Networks and Systems*, Hrsg. Radek Silhavy und Petr Silhavy, 15–25. https://doi.org/10.1007/978-3-031-35314-7_2.

Nawfal Mustafa M, 2021. Classification of maintenance techniques and diagnosing failures methods. *Journal of Physics: Conference Series,* 2060: 012014. https://doi.org/10.1088/1742-6596/2060/1/012014.

Odhiambo Omuya E, Onyango Okeyo G, Waema Kimwele M, 2021. Feature Selection for Classification using Principal Component Analysis and Information Gain. *Expert Systems with Applications,* 174: 114765. https://doi.org/10.1016/j.eswa.2021.114765.

Raj KK, Kumar S, Kumar RR, 2025. Systematic Review of Bearing Component Failure: Strategies for Diagnosis and Prognosis in Rotating Machinery. *Arabian Journal for Science and Engineering,* 50: 5353–5375. https://doi.org/10.1007/s13369-024-09866-x.

Tang Y, Zhang C, Wu J, et al., 2024. Deep Learning-Based Bearing Fault Diagnosis Using a Trusted Multiscale Quadratic Attention-Embedded Convolutional Neural Network. *IEEE Transactions on Instrumentation and Measurement,* 73: 1–15. https://doi.org/10.1109/TIM.2024.3374311.

Wan L, Gong K, Zhang G, et al., 2021. An Efficient Rolling Bearing Fault Diagnosis Method Based on Spark and Improved Random Forest Algorithm. *IEEE Access,* 9: 37866–37882. https://doi.org/10.1109/ACCESS.2021.3063929.

Wang B, Qiu W, Hu X, et al., 2024. A rolling bearing fault diagnosis technique based on recurrence quantification analysis and Bayesian optimization SVM. *Applied Soft Computing,* 156: 111506. https://doi.org/10.1016/j.asoc.2024.111506.

Wang X, Zheng J, Ni Q, et al., 2022. Traversal index enhanced-gram (TIEgram): A novel optimal demodulation frequency band selection method for rolling bearing fault diagnosis under non-stationary operating conditions. *Mechanical Systems and Signal Processing,* 172: 109017. https://doi.org/10.1016/j.ymssp.2022.109017.

Wang Z, Huang H, Wang Y, 2021. Fault diagnosis of planetary gearbox using multi-criteria feature selection and heterogeneous ensemble learning classification. *Measurement,* 173: 108654. https://doi.org/10.1016/j.measurement.2020.108654.

Yang D, Wang X, Wang Y, et al., 2019. A multi-source fusion algorithm for high-accuracy signal reconstruction of vehicle interior noise on passenger ear-sides. *Applied Acoustics,* 148: 75–85. https://doi.org/10.1016/j.apacoust.2018.12.017.

Yao J, Liang W, Duan L, et al., 2025. Non-contact intelligent diagnosis method for key components in energy equipment based on acoustic signal and deep learning. *Applied Energy,* 398: 126380. https://doi.org/10.1016/j.apenergy.2025.126380.

Yue C, Zhu Y, Cheng P, et al., 2024. A Novel Method for Identifying Resonance Frequency Band in Weak Bearing Fault Diagnosis of Electric Driving System. *Shock and Vibration,* 2024: 2804173. https://doi.org/10.1155/2024/2804173.

Yue C, Dong J, Zhu Y, et al., 2025. A novel fault diagnosis model for rolling bearings in electric drive systems using multi-scale improved weighted permutation entropy and radial basis function neural network. *Insight - Non-Destructive Testing and Condition Monitoring,* 67: 39–46. https://doi.org/10.1784/insi.2025.67.1.39.

Zhang X, Han P, Xu L, et al., 2020. Research on Bearing Fault Diagnosis of Wind Turbine Gearbox Based on 1DCNN-PSO-SVM. *IEEE Access,* 8: 192248–192258. https://doi.org/10.1109/ACCESS.2020.3032719.

Zhao J, Wang W, Huang J, et al., 2025. A comprehensive review of deep learning-based fault diagnosis approaches for rolling bearings: Advancements and challenges. *AIP Advances,* 15: 020702. https://doi.org/10.1063/5.0255451.

中文概要

题　　目：基于多源特征融合筛选机制的电驱系统微弱故障特征诊断方法

作　　者：岳聪、康竞文、赵永昊、程萍

机　　构：上海海事大学，物流工程学院，中国上海，201306

目　　的：电动驱动系统（EDS）具备高度集成化与非线性特征，导致系统微弱故障识别难度较大，同时非接触式故障监测的声学质点振速信号易受噪声与冗余特征干扰，严重影响微弱故障特征提取效果，降低故障诊断稳定性。本文旨在克服传统单特征、多特征筛选方法的局限性，探究高效的特征融合筛选方式，增强微弱故障特征表征能力，提升电动驱动系统微弱故障诊断的精度、稳定性与泛化性能。

创新点：1. 针对 EDS 采集的声学信号存在噪声干扰强、冗余特征多、微弱故障难以提取的问题，提出一种基于信息熵的多源特征筛选机制（IE-MSFS）；2. 利用基于质点振速的声学信号开展故障诊断研究，并与传统低质量和高质量振动信号进行对比验证，有效提升微弱故障诊断的稳定性与准确性。

方　　法：1. 采用基于改进信息熵的多源特征融合选择（IE-MSFS）方法，剔除 EDS 声学质点振速信

号中冗余的噪声干扰信息，增强微弱故障特征的表征能力；2. 采集实验室环境下的 EDS 声学信号，结合机器学习算法，对三种典型微弱故障类型开展诊断测试，并与振动信号诊断结果进行对比分析；3. 通过多组试验测试，验证所提故障诊断模型（CIR-PS）在微弱故障诊断中的识别性能、鲁棒性和泛化能力。

结　　论：(1) 提出了一种新的特征筛选方法（IE-MSFS），用于解决微弱故障诊断中的噪声干扰和冗余问题。该方法基于 IMF 分量的进行多源特征融合筛选，以抑制冗余特征，并在噪声条件下增强微弱故障特征的表征能力。(2) 基于所提出的 IE-MSFS 方法，利用三组典型的 EDS 微弱故障声学信号对 CIR-PS 模型进行验证。在不同信噪比条件下的证实了该模型出色的抗噪声鲁棒性，故障诊断准确率高于 95.2%。（3） 对两种振动信号数据集的验证表明，CIR-PS 模型能够有效区分内圈和外圈的微弱故障。其最低准确率均超过 96.4%，表现出优异的泛化能力了和实用性。

关键词：质点振速信号；微弱故障诊断；多源融合特征筛选机制；增强特征提取